A high-fidelity model of the human heart: an immersed boundary implementation

Francesco Viola,[1,2] Giulio Del Corso,[1,*] and Roberto Verzicco[1,3,4,†]

[1] *GSSI, Viale Francesco Crispi 7, 67100, L'Aquila, Italy*
[2] *INFN-Laboratori Nazionali del Gran Sasso, Assergi (AQ), Italy.*
[3] *Physics of Fluids Group, University of Twente, 7500AE Enschede, The Netherlands*
[4] *Dipartimento di Ingegneria Industriale, University of Rome 'Tor Vergata', Roma 00133, Italy*

(Dated: August 23, 2023)

Computer simulations of cardiovascular flows can be key to improve the predicting capabilities of standard diagnostic tools, to refine surgical techniques and perform virtual tests of innovative prosthetic devices. The reliability of simulations, however, depends on the fidelity level of the model which, for the heart, involves the interconnected multi–physics dynamics of the various systems: the human heart is among the most complex organs and simulating its dynamics is an ambitious undertaking both, from the modeling and computational viewpoints.

In this paper we present a multi–physics computational model of the human heart accounting simultaneously for the electrophysiology, the elasto–mechanics and the hemodynamics, including their multi–way coupled interactions referred to as fluid–structure–electro interaction (FSEI). The developed tool embodies accuracy, versatility and computational efficiency thus allowing cardiovascular simulations of physiologic and pathologic configurations within a time–to–solution compatible with the clinical practice and without resorting to large–scale supercomputers.

Results are shown for healthy conditions and for myocardial infarction with the aim of assessing the reliability of the model and proving its predicting capabilities which could be used to anticipate the outcome of surgical procedures or support clinical decisions.

I. INTRODUCTION

The term 'digital twins' indicates virtual models which accurately duplicate the dynamics of a physical object; actually, they are nothing but sophisticated computer programs designed and tuned (or trained) to reproduce, with high–fidelity, selected features of a mimicked system [1]. In the last decade, cardiovascular digital twins have experienced impressive improvements in complexity and reliability and they are among the most promising candidates to stimulate the next breakthrough in modern medicine. In fact, they provide innovative tools for the diagnosis and prognosis of cardiovascular disorders (CVD), which are the main cause of death and health care costs in developed countries [2]. Nowadays, computational engineering allows for the virtual reconstruction of the cardiac system along with the simulation of its complex dynamics so as to add predicting capabilities to the actual diagnostic devices and improve the precision of many evidence based current clinical procedures. On the other hand, accurate and reliable CVD simulations involve the interconnected multi–physics dynamics of the various heart systems and their simulation entails huge modeling and computational work. Early attempts of cardiovascular models started from specific parts, like valves, heart chamber electrophysiology or tracts of veins and arteries [3–8] and only recently, when computers have become powerful enough, larger portions of the system have been tackled [9–13].

The human heart is a hollow muscular organ which pumps blood throughout the body, to the lungs and to its own tissue through the systemic–, pulmonary– and coronary–circulation, respectively. The heart achieves these fundamental goals by two pumps in series, the right and the left, which beat (almost) synchronously 2–3 billion times during lifetime to deliver a mean flow rate of about 5 l/min using an amount of power of only ≈ 8 W with an outstanding reliability. This astonishing performance is obtained through the highly synergistic and interconnected dynamics of different systems which cooperate to yield the optimized operation: these are ı) the electrophysiologic system, ıı) the active muscular tissue with the passive valves and ıı) the flowing blood. The 'orchestra conductor' of this complex dynamics is the electrophysiologic system which coordinates timings and delays of contraction and relaxation of different myocardium regions in order to assure the efficient pumping action [14].

In a nutshell, the electrical signal originates from the sinoatrial node (figure 1a), which gives the pace of the heartbeat. From there, it propagates through the atria within ≈ 100 ms, thus depolarising the muscle myocytes and inducing their contraction. When the signal reaches the atrioventricular node, it is delayed by ≈ 100 ms to allow the relaxed ventricles to be properly filled by the final atrial systole. The signal then quickly moves through the

* Present address: Institute of Information Science and Technologies A. Faedo, CNR, Pisa, Italy
† roberto.verzicco@gssi.it

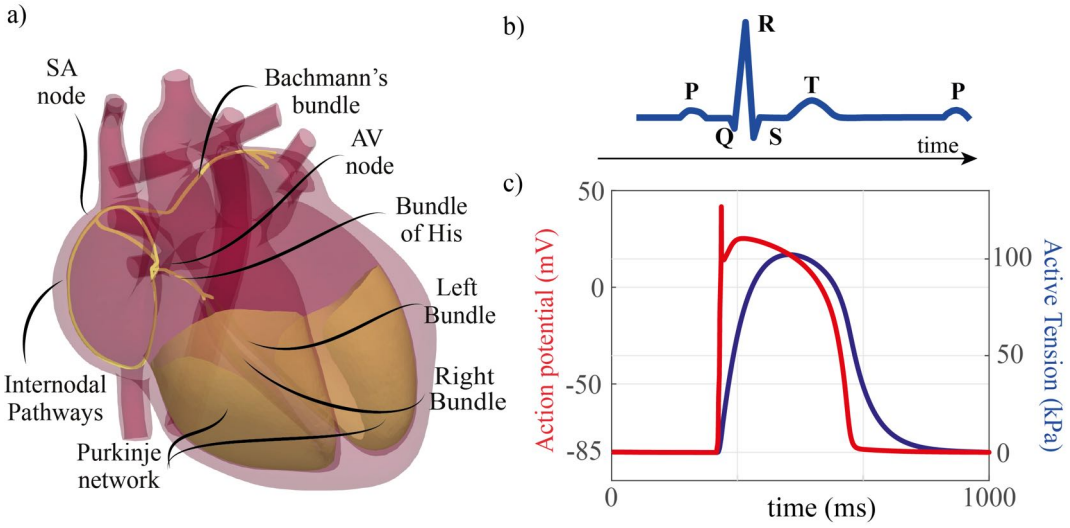

FIG. 1. a) Perspective vies of the heart with the electrophysiology system and its main structures. b) Main elements of the ECG trace. c) Schematic relation between activation electrical potential and axial tension for a myocyte cell.

bundle of His and then to the Purkinje fibers to trigger, in less than ≈ 300 ms, the vigorous ventricular contraction which is responsible for the pumping action. The depolarisation of atria and ventricles corresponds, respectively, to the P wave and QRS complex in the electrocardiogram (ECG) trace (figure 1b), whereas the T wave indicates the ventricles ripolarisation which gives a relaxed state. Although each heart region has different myocytes, a general behavior is shown in figure 1c: when the electrical signal reaches a myocyte, the local transmembrane potential rapidly jumps from the negative resting value of about -85 mV, to a positive value of about 20 mV which is maintained for about 200 ms. This transient depolarization produces an active tension along the axis of the myocytes organized into muscular fibers which align in specific directions to form the anisotropic myocardial tissue. Its periodic contraction and relaxation generates a strongly three–dimensional, pulsatile flow driving the blood from atria to ventricles and then to the arteries; the correct flux direction is assured by the passive opening/closing of the cardiac valves. Furthermore, the hydrodynamic loads acting on the wet surfaces force the kinematics of the myocardium and of the cardiac valves that are known to have nonlinear and anisotropic elastic properties.

Tackling the complexity of the whole heart is clearly a formidable computational task and this paper describes some recent progress made in this direction. We present a multi–physics computational approach capable of simulating simultaneously the electrophysiology, the elasto–mechanics and the fluid dynamics of the heart, including their multi–way coupled interactions. The developed model exhibits accuracy, versatility and computational efficiency, thus allowing for cardiovascular simulations in physiologic conditions without entailing exorbitant computational resources.

During its development, the various software modules have been validated through comparisons with clinical data, results from the literature and ad–hoc experiments [15–18]; here we present the latest developments of the multi–coupled fluid–structure–electro interaction (FSEI) algorithm [18] with improved realism of the human heart and, more important, augmented predictive capabilities of the cardiac dynamics.

The model lies on three pillars: a fluid solver for the pulsatile hemodynamics evolving in a complex–geometry, deforming domain; a structure solver for the anisotropic hyperelastic biological tissues with a dynamics determined both by active tension and hydrodynamic loads; and an electrophysiology solver, for the propagation of the activation potential through the organ, which accounts for the hierarchical 1D, 2D and 3D structures of the system.

After having described the main features of the computational tool, it will be employed to reproduce the physiology of healthy and impaired hearts owing to the presence of an ischemic region in the left ventricular myocardium.

The paper is organized as follows: § 2 introduces the problem, the configuration of the heart and its main systems. § 3 describes the governing equations of the these systems, the coupled electro–fluid–structure interaction and some technicalities of the numerical methods. The results obtained for healthy and pathologic configurations are presented and discussed in § 4. Finally, closing remarks and future perspectives are given in § 5.

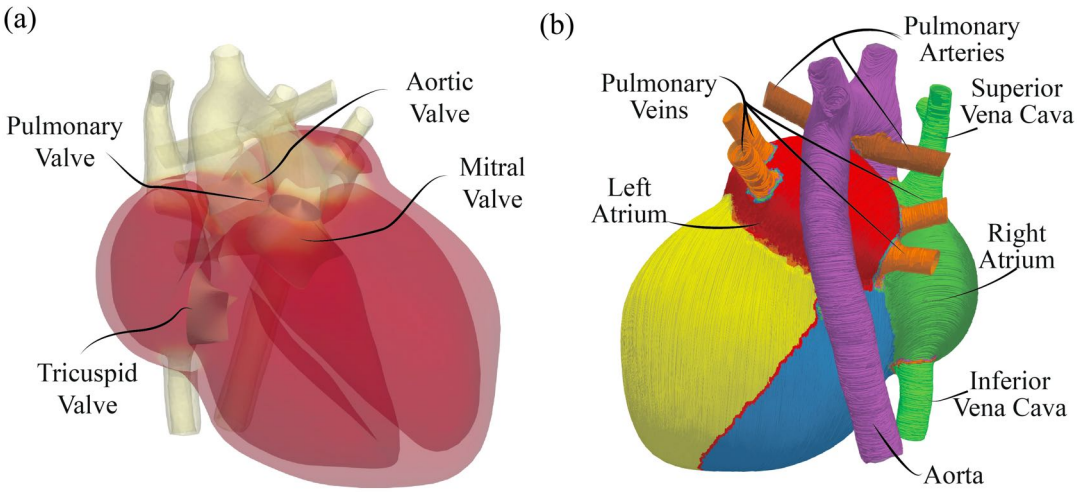

FIG. 2. Structure of the heart used for the simulations: a) valves and chambers; b) Tagging of the different regions and local orientation of the fibers. The main parameters in diastole are: left ventricle (LV) long axis 92 mm; LV short axis 50 mm; right ventricle (RV) long axis 79 mm; RV short axis 32 mm; left atrium (LA) volume 75 ml; right atrium (RA) volume 84 ml. Aortic annulus diameter 23 mm; Pulmonary annulus diameter 22 mm; Mitral ostium area 800 mm^2; Tricuspid ostium area 800 mm^2. Additional details are given in [20].

II. THE PROBLEM

Given the extreme human variability, even the definition of a typical heart configuration is a problem in its own right [19]. For example, among healthy adults the maximum (end diastolic) left–ventricle volume is in the range 75–211 ml and the ejected (stroke) volume 45–125 ml; all other geometrical dimension have similar variations [20] thus making uncertain the definition of a representative heart. A popular choice consists of using the so–called 'patient specific' geometries, extracted from computed tomography (CT) scans, which can be employed to answer precise questions or to plan the surgery for a single individual. In this case the geometry of the heart reflects precisely that of the specific patient although all the tissues mechanical properties and the conduction parameters of the electrophysiology system have to be indirectly estimated or assumed from reference values.

In our study we pursue a different approach in which we use an idealized heart having the average properties of a large cohort of patients [20]. More in detail, we have extracted from the literature the ensemble–average of the main dimensions of each heart chamber, valve and main vessel, to assemble a *standard* heart which is representative of a broad class of humans although of none of them in particular: the result is shown in figure 2.

Oxygenated blood enters the left atrium via the pulmonary veins and flows into the left ventricle crossing the open bileaflet mitral valve during diastole. During systole, the ventricle contracts, increasing blood pressure therein, and when it exceeds the value in the aorta (about 80 mmHg in healthy adults) the aortic valve opens and blood is squeezed into the aorta. Concurrently, the upper and lower venae cavae collect CO_2 saturated blood from the body and direct it to the right atrium. Blood is then routed to the right ventricle through the open tricuspid valve which closes during systole as blood pressure increases and blood is pumped to the common tract of the pulmonary arteries across the pulmonary valve.

The contraction of all the muscular tissue (myocardium) is active and triggered by the activation potential of the electrophysiology system while the motion of the heart valves is passive and governed by the hydrodynamic loads only. Heart chambers are modeled as a single elastic 3D medium with position–dependent, nonlinear, anisotropic elastic properties; also the myocardium thickness and orientation of the muscular fibers is a local property and they reflect the heart physiology. Note that, as the embryological heart development entails loopings and foldings of elementary layers of tissue, in the ventricles the orientation of the fibers is inhomogeneous across the myocardium thickness [21] and also this property is considered in our model.

All the heart valves, consisting of thin leaflets of passive connective tissue, are modeled as 2D membranes with some bending stiffness to avoid surface wrinkling.

In our simulations the heart rate is set to 70 beats-per-minute (bpm) corresponding to a period of $T = 857.1$ ms and in a typical run temporal integration is performed over 6 heart beats: the first is discarded since it accommodates the initial transient with the pretensioning of all tissues while the remaining ones are used to compute phase–averaged statistics.

	Ω_{ao}	Ω_{epi}	Ω_{pv}	Ω_{pa}	Ω_{vcs}	Ω_{vci}
α_{wk} (Kg m^{-3}s^{-1} $\times 10^6$)	3.13	16.62	0.062	0.78	0.39	0.39
β_{wk} (Kg m^{-3}s^{-2} $\times 10^6$)	2.96	10.36	0.059	1.18	0.11	0.11
γ_{wk} (Kg m^{-2}s^{-2} $\times 10^6$)	18.43	25.68	0.00	4.17	0.00	0.00

TABLE I. Windkessel parameters at the inlets/outlets of the cardiac model.

As we will detail in the next section, the hemodynamics developing in the complex, deformable shape of the heart is dealt with by an Immersed Boundary (IB) method [4, 22] thus the whole geometry is placed in a Cartesian computational domain where the Navier–Stokes equations are integrated and the no–slip condition on all wet surfaces is imposed through body forces. The domain size is $l_x \times l_y \times l_z = 100 \times 100 \times 140$ mm^3 and it is discretized by a uniform mesh of, at least, $531 \times 531 \times 751$ nodes corresponding to a grid spacing $\Delta \leq 190$ μm. This fine mesh and the stiffness of the coupled system of equations enforces an integration time step of $\Delta t \approx 2$ μs implying about half a million of time steps to advance each heartbeat.

All the circulations of the human body form a self connected hydraulic circuit with the blood flowing in a closed loop; our computational domain, however, accounts only for the heart and the initial tract of the main vessels thus all the missing circulations have to be mimicked by suitable boundary conditions capable of reproducing the appropriate impedance on the flow. To this aim, each distal end of veins and arteries is embedded in a cylindrical volume where additional volume forces, in the form $\mathbf{f}_{wk} = \alpha_{wk}\mathbf{u} + \beta_{wk}\int_0^t \mathbf{u}(\tau)\mathrm{d}\tau + \gamma_{wk}\mathbf{n}_\Omega$, are added to the Navier–Stokes equations. These are equivalent to a three–element Windkessel [23–25] with specific constants α_{wk}, β_{wk} and γ_{wk} at each distal end as detailed in [20]: here we report the numerical values in Table I for the ease of reading.

It is worth mentioning that these boundary condition parameters for each artery and vein have been tuned, through preliminary simulation, so as to yield the physiological pressure and flowrate waveforms; they are therefore not predictions of the model but rather input data needed to obtain the correct dynamics within the heart.

III. MODELS AND GOVERNING EQUATIONS

In this section we present each model, together with the related equations, used to build the multi–physics digital twin of the heart. We describe separately the fluid–, electrophysiology– and structural–solvers, along with their coupling. Detailed descriptions and thorough validations can be found in [18, 20, 26, 27], here only the main methodological novelties of the computational set–up are highlighted.

A. Flow solver

Blood velocity $\mathbf{u}$ and pressure p are governed by the Navier–Stokes and continuity equations for an incompressible, viscous flow which, in non–dimensional form, read:

$$\begin{aligned} \frac{\partial \mathbf{u}}{\partial t} + \mathbf{u}\cdot\nabla\mathbf{u} &= -\nabla p + \nabla\cdot\boldsymbol{\tau} + \mathbf{f}, \\ \nabla\cdot\mathbf{u} &= 0. \end{aligned} \tag{1}$$

$\boldsymbol{\tau}$ is the viscous stress tensor which, in our model, depends on the strain–rate tensor $\boldsymbol{E} = (\nabla\mathbf{u} + \nabla^T\mathbf{u})/2$ through a Carreau–Yasuda shear–thinning model, as described in [28]. However, the non–Newtonian features of blood become dominant only in sub–millimetric vessels while, as shown in [29], the flow developing in larger structures can be modeled by a Newtonian constitutive relation unless particular phenomena, like hemolysis, have to be considered. Accordingly, in this study, the linear constitutive relation $\boldsymbol{\tau} = 2\boldsymbol{E}/Re$ has been used for all simulations thus imposing a fluid viscosity independent of the rate–of–strain. The Reynolds number is defined using the effective kinematic viscosity for human blood with an hematocrit of 40%, $\nu = 4.8 \times 10^{-6}$ m^{2}s^{-1}, $d^m = 3.2$ cm the mitral annulus diameter and $U^m = 60$ cm/s the average velocity through the mitral annulus during diastole measured using Doppler echocardiography: the resulting value is $Re = U^m d^m/\nu = 4000$ which will be used for all simulations.

The governing equations (1) are numerically solved as in [18], using the AFiD solver based on central, second–order, finite–differences on a staggered mesh for spatial discretization [30–32]. As mentioned above, the heart is placed in a Cartesian computational domain and the no–slip condition on the wet surfaces is imposed using an IBM technique

based on the moving least square (MLS) approach [33, 34]. Given $\mathbf{u}^n$ and p^n, velocity and pressure fields at time t^n, and Δt the time step, the provisional non–solenoidal velocity field $\hat{\mathbf{u}}$ satisfies:

$$\frac{\hat{\mathbf{u}} - \mathbf{u}^n}{\Delta t} = -\alpha \nabla p^n + \gamma H^n + \rho H^{n-1} + \frac{\alpha}{2Re} \nabla^2 (\hat{\mathbf{u}} + \mathbf{u}^n), \tag{2}$$

where H incorporates the nonlinear terms and some volume forces while $\gamma = 3/2$, $\rho = -1/2$ and $\alpha = \gamma + \rho = 1$ are the coefficients of the Adams–Bashforth/Crank–Nicolson time advancement scheme [35].

The no–slip condition on the wet surfaces is imposed at the Lagrangian markers uniformly distributed on the immersed boundaries and then transferred to the Eulerian gridpoints as shown in figure 3.

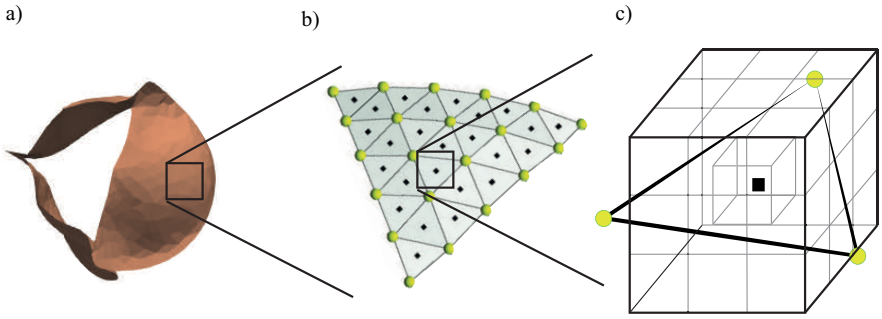

FIG. 3. IB treatment of the deformable tissues. (a) Generic wet surface, (b) triangulated mesh with the mass concentrated at the nodes and the Lagrangian markers placed at its centroids, (c) support domain around a Lagrangian marker consisting of 27 Eulerian cells.

A three–dimensional support domain ('cage') consisting of $N_e = 3 \times 3 \times 3 = 27$ Eulerian nodes is created around each Lagrangian marker and the fluid velocity therein $\hat{\mathbf{u}}(\mathbf{x}_b)$ is computed through interpolation using the velocity at the N_e Eulerian points of the cage

$$\hat{u}_i(\mathbf{x}_b) = \sum_{k=1}^{N_e} \phi_i^k(\mathbf{x}_b) \hat{u}_i(\mathbf{x}_k), \tag{3}$$

$\phi_i^k(\mathbf{x})$ are the transfer operators which depend on the shape functions used for the interpolation. Generally, this interpolated velocity does not match with that of the corresponding Lagrangian marker $\mathbf{u}_b(\mathbf{x}_b)$ and their difference is therefore used to compute a source term $\mathbf{f}_b = [\mathbf{u}_b(\mathbf{x}_b) - \hat{\mathbf{u}}]/\Delta t$ which is then transferred back to the Eulerian grid points as a distributed forcing $\mathbf{f}$ by a relation similar to (3). This procedure is repeated for all Lagrangian markers and the resulting forcing field is used to update the provisional velocity $\hat{\mathbf{u}}$ as

$$\mathbf{u}^* = \hat{\mathbf{u}} + \Delta t \mathbf{f}. \tag{4}$$

Since $\mathbf{u}^*$ is still a non–solenoidal field it is projected onto a divergence–free space by a correction in the form

$$\frac{\mathbf{u}^{n+1} - \mathbf{u}^*}{\Delta t} = -\alpha \nabla \Phi \qquad \Rightarrow \qquad \mathbf{u}^{n+1} = \mathbf{u}^* - \alpha \Delta t \nabla \Phi, \tag{5}$$

where the scalar field Φ comes from the elliptic equation $\nabla^2 \Phi = \nabla \cdot \mathbf{u}^* / (\alpha \Delta t)$ which yields also the updated pressure through

$$p^{n+1} = p^n + \Phi - \frac{\alpha \Delta t}{2Re} \nabla^2 \Phi. \tag{6}$$

It should be noted that the projection step (5), enforcing the divergence–free condition for the velocity $\mathbf{u}^{n+1}$, slightly perturbs the field $\mathbf{u}^*$ which satisfies the IB condition imposed in step (4). In order to reduce a residual mass flux through the immersed surfaces, the steps (4) and (5) may be iterated to obtain an updated velocity $\mathbf{u}^{n+1}$ complying, at the same time, with the solenoidal– and the no–slip boundary–condition up to a given tolerance: typically one or two iterations are sufficient to yield the desired convergence for the valve leaflets and four for pressurized heart chambers.

Hydrodynamic loads are needed as input for the structural solver thus pressure and viscous stresses are evaluated at the Lagrangian markers laying on the immersed body surface. For the valve leaflets, both surface sides are wet

by the flow and the local force at each triangular face $\mathbf{F}_f^{ext}$ is computed along positive $\mathbf{n}^+$ and negative $\mathbf{n}^- = -\mathbf{n}^+$ normal directions:

$$\mathbf{F}_f^{ext} = [-(p_f^+ - p_f^-)\mathbf{n}_f^+ + (\boldsymbol{\tau}_f^+ - \boldsymbol{\tau}_f^-) \cdot \mathbf{n}_f^+]A_f, \tag{7}$$

A_f is the area of the surface. In contrast, for closed surfaces, like heart chambers and vessels, hydrodynamic loads are computed only on one side of the surface.

$$\mathbf{F}_f^{ext} = [-p_f \mathbf{n}_f + \boldsymbol{\tau}_f \cdot \mathbf{n}_f]A_f, \tag{8}$$

where $\mathbf{n}_f$ is the outward normal vector of the wet surface. The hydrodynamic loads, evaluated at the baricentric Lagrangian markers, are then transferred to the triangle nodes according to

$$\mathbf{F}_n^{ext} = \frac{1}{3}\sum_{i=1}^{N_{nf}} \mathbf{F}_{fi}^{ext} A_{fi}, \tag{9}$$

N_{nf} being the number of faces sharing the node n and $\mathbf{F}_{fi}^{ext}$ and A_{fi} hydrodynamic forces and surfaces of the i–th face sharing the node n.

It must be noted that, differently from valve leaflets, atria and ventricles are three–dimensional structures, with a finite–thickness myocardium, wet by the blood only on the side lined by the endocardium; this implies that IB force (4) and external loads (9) should be computed only at the corresponding surface. To this aim, the triangular faces belonging to the endocardium are identified in a pre–processing step and tracked in time (see figure 4a), thus providing the instantaneous position of the wet surface needed for fluid/structure interaction, as shown in panels (b) and (c) for systole and diastole, respectively.

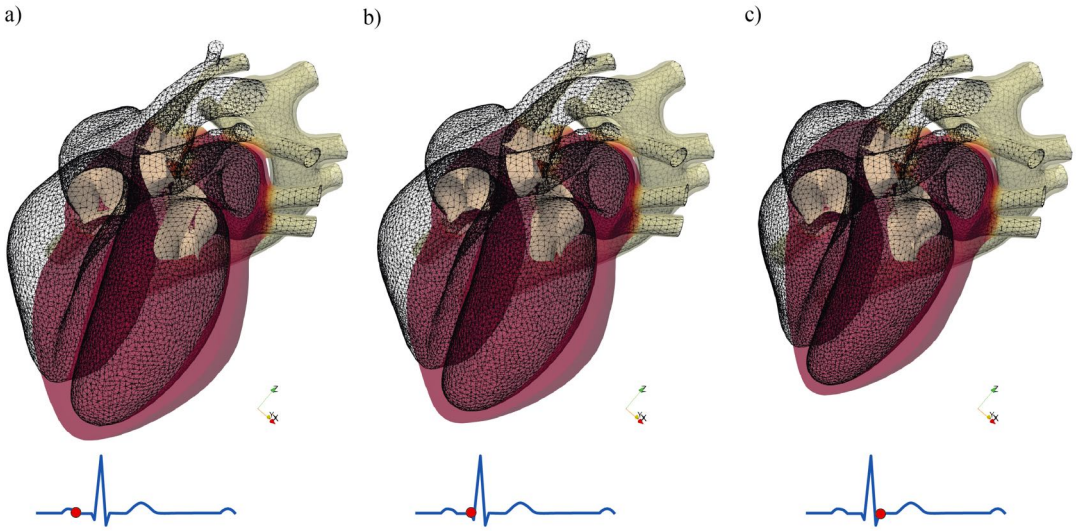

FIG. 4. Snapshots of the three–dimensional myocardium and the corresponding two–dimensional endocardium wet by the blood flow during different phases of the cycle.

1. *Adaptive tiling rule*

The two–way transfer between Lagrangian and Eulerian grids requires that each grid cell crossed by the immersed boundary can be associated (at least) with a surface triangle. If the triangulation is too fine and more than one surface element fits into a single mesh volume, only the triangle whose centroid is closest to the Eulerian variable will be used to compute the IB forcing with the remaining ones staying 'idle'. Viceversa, with a too coarse triangulation, a single surface element will cross several mesh volumes and only that closest to the triangle centroid will have the Lagrangian information transferred: all the other mesh elements will be 'orphan' and do not guarantee the correct imposition of boundary conditions by IB forcings. Of course, the first possibility still provides a correct solution, although computing resources are wasted with idle triangles; on the other hand, in the second case, orphan cells

will produce fluid flow across the immersed boundary which will spoil the solution. [35] have shown that a working compromise between the above opposite instances is to have a surface triangulation with equilateral triangles having edges of size ≈ 0.7 times the local grid spacing; this choice does not penalize the computational overhead while assuring the absence of orphan mesh nodes.

An immediate consequence of these constraints is that as the Eulerian grid is refined, also the Lagrangian resolution must be increased thus entailing geometry remeshing for every change of Eulerian resolution. In the present case, the problem is further exacerbated by the periodic myocardium contraction, almost halving ventricular volumes at the end of systole with respect to their end–diastolic values, which shrinks and stretches the surface triangles and varies the Lagrangian–to–Eulerian mesh size ratio from the initial design 0.7 to sub–optimal values.

These problems are prevented by using an adaptive Lagrangian mesh refinement procedure where the initial triangular mesh is automatically subdivided into virtual subtriangles (the 'tiles') until each one gets smaller than the local Eulerian grid size, thus avoiding 'holes' in the interfacial boundary condition. In this way, heart tissues can be discretized independently of the Eulerian mesh and each triangle is successively refined until the Lagrangian resolution of the tiled surface is sufficiently fine. The tiling procedure can be run either once at the beginning of the simulation or dynamically at each time step according to the instantaneous tissue deformation that change the local ratio between Lagrangian and Eulerian grids. As discussed also in [18] the advantage of an adaptive refinement of the Lagrangian triangulation for high Reynolds number flows is twofold: on one hand it allows the use of the same base triangulation regardless of the Eulerian grid and, on the other, the number of Lagrangian nodes used to deform the immersed body can be reduced, provided that the structural loads are accurately resolved.

A possible tiling approach is the barycentric adaptive rule [36] consisting of splitting the triangles into three parts according to the medians passing through the centroid. Higher Lagrangian resolution can thus be obtained by successive splitting of the subtriangles according to the same procedure (figure 5a). The barycentric tiling rule, however, has two main drawbacks: the shape of the tiles changes with respect to the initial triangle and it gets more skewed as successive tiling steps are made (see figure 5a). Furthermore, the number of tiles increases exponentially $N_{tiles} = 3^b$ with the tiling step b (figure 5d) and this limits the flexibility of the procedure as the Lagrangian resolution can only be increased by powers of 3 and so does the computational cost of the IB-MLS.

These shortcomings are mitigated by an adaptive quadratic tiling [18, 37] where triangles are tiled by tracing a set of $m-1$ (with $m = 1, 2, 3\dots$) equispaced lines parallel to each triangle edge intersecting the other two. According to Talete's theorem all tiles are similar to the original triangle and, consequently, are similar among each other. Moreover, the number of tiles grows algebraically $N_{tiles} = m^2$ with the tiling steps m, thus allowing a greater control of the Lagrangian resolution with respect to the barycentric tiling rule. This last aspect can be further improved by combining the quadratic tiling rule with the barycentric one. Specifically, both strategies are used to split the triangles with the number of barycentric and quadratic steps (b and m, respectively) which can be varied independently so as to obtain the desired Lagrangian refinement. The resulting 'mixed' rule, hence, provides a richer space of tiling configurations (figure 5c) with the number of tiles growing slower than respect for the other strategies (figure 5d).

B. Electrophysiology

The functioning of individual myocyte cells is known in detail under normal or pathological conditions [38–40] and computational models of increasing complexity have been conceived to link specific molecular mechanisms to cellular physiology [41, 42]. Unfortunately, the number of myocytes in the heart is intractable (there are more than 5 billions of them in the left ventricle only [43]) and reproducing the cardiac electrophysiology starting from the single cell is currently out of reach. In order to overcome this limitation, effective myocardium models have been formulated using a continuum medium made of intracellular and extracellular overlapping domains separated by a distributed membrane [44, 45]: these are referred to as 'bidomain models' and are widely used in many different contexts. The electric potential difference across the domains (v, transmembrane potential) and the extracellular potential (v_{ext}) satisfy a generalized Ohm law which can be written as:

$$\begin{aligned} \chi\left(C_m\frac{\partial v}{\partial t} + I_{ion}(\mathbf{s}) + I_s\right) &= \nabla\cdot(M^{int}\nabla v) + \nabla\cdot(M^{int}\nabla v_{ext}),\\ 0 &= \nabla\cdot(M^{int}\nabla v + (M^{int}+M^{ext})\nabla v_{ext}),\\ \frac{\mathrm{d}\mathbf{s}}{\mathrm{d}t} &= F(\mathbf{s}, v, t) \end{aligned} \tag{10}$$

where the surface–to–volume ratio of cells, χ, and the specific membrane capacitance C_m are set as in [18] equal to $\chi = 1400\ \mathrm{cm}^{-1}$ $C_m = 1\mu\mathrm{F\ cm}^{-2}$, respectively. M^{int} and M^{ext} are the conductivity tensors of the intracellular and extracellular media, which reflect the orthotropic myocardium electrical properties and depend on the local fiber

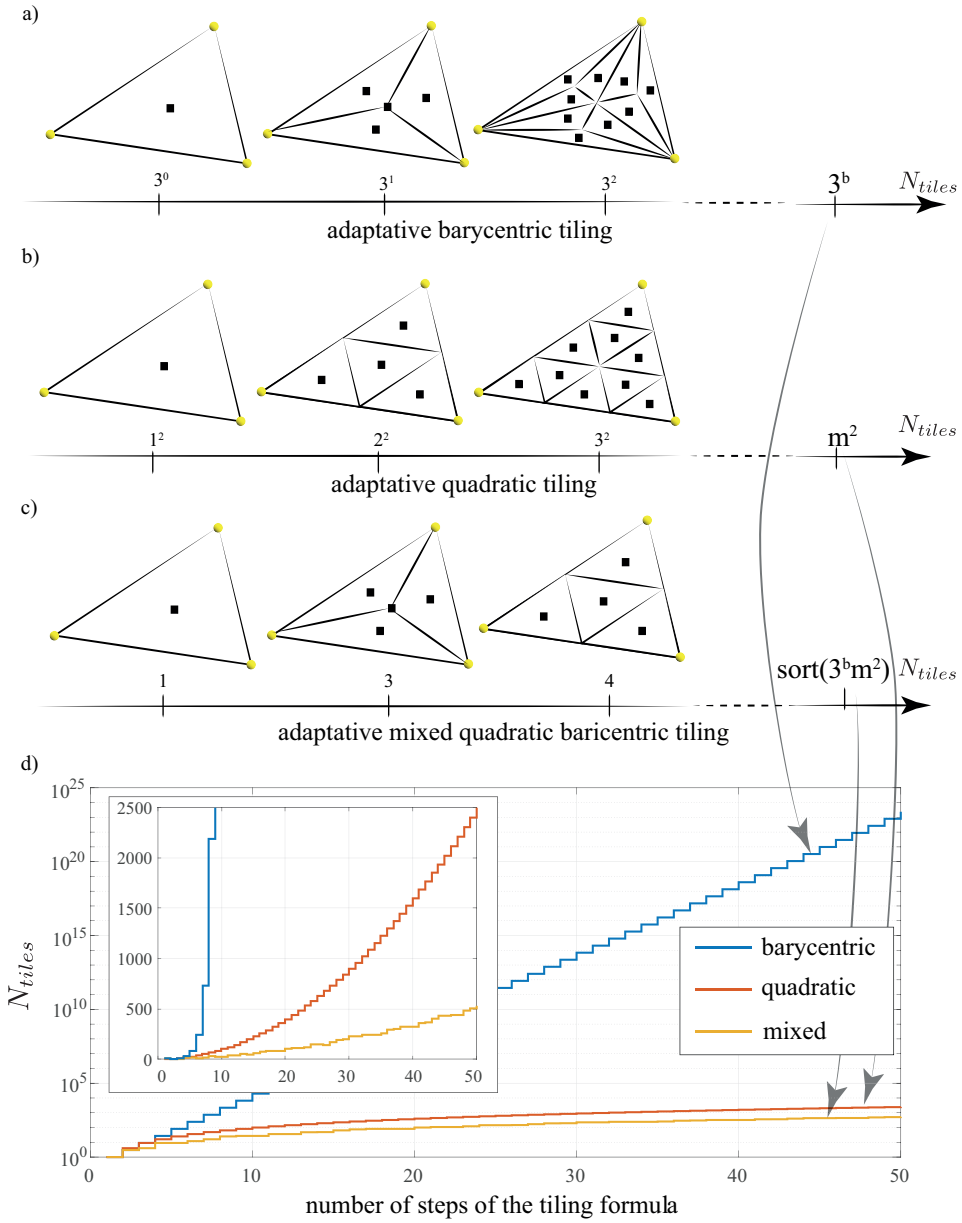

FIG. 5. Possible adaptive tiling strategies. (a) Barycentric (b) quadratic and (c) mixed quadratic/barycentric formula, along with the corresponding (d) number of tiles as a function of the number of steps of the formula. A slower growth in the last panel corresponds to a better control of the Lagrangian resolution through the adaptive tiling.

orientation, since the propagation velocity is faster along the muscle fiber than in the cross–fiber directions. Expressed in the basis formed by the fiber, sheet and sheet–normal directions the local conductivity tensors $\hat{M}^{ext}$, $\hat{M}^{int}$ are diagonal [46]

$$\hat{M}^{ext} = \begin{bmatrix} m^{ext,f} & 0 & 0 \\ 0 & m^{ext,s} & 0 \\ 0 & 0 & m^{ext,n} \end{bmatrix}, \qquad \hat{M}^{int} = \begin{bmatrix} m^{int,f} & 0 & 0 \\ 0 & m^{int,s} & 0 \\ 0 & 0 & m^{int,n} \end{bmatrix}, \tag{11}$$

and the non–null diagonal components are the principal conductivities, which are set as in [20]. The conductivity tensor in the global coordinate system are thus obtained by the transformation

$$M^{ext} = \mathcal{A}\hat{M}^{ext}\mathcal{A}^T, \qquad M^{int} = \mathcal{A}\hat{M}^{int}\mathcal{A}^T, \tag{12}$$

where $\mathcal{A}$ is the rotation matrix containing column–wise the components of fiber, sheet and sheet–normal unit vectors

$$\mathcal{A} = \begin{bmatrix} e_{f,x} & e_{s,x} & e_{n,x} \\ e_{f,y} & e_{s,y} & e_{n,y} \\ e_{f,z} & e_{s,z} & e_{n,z} \end{bmatrix}. \tag{13}$$

The quantity $I_{ion}(\mathbf{s})$, in the first of equations (10), is the ionic current per unit cell membrane (measured in $\mathrm{mA{\cdot}mm^{-2}}$) which is determined by the state vector $\mathbf{s}$ given by the cellular model (the last of equations (10)). Different heart tissues entail different myocytes described by specialized cell models: the Courtemanche model [38] has been used for the atrial myocytes, the Stewart model [39] for the Purkinje network and the ten Tusscher–Panfilov model [40] for the ventricular myocytes. Lastly, I_s is a prescribed input current needed to initiate the electrical propagation which in the heart is generated by specialized self–oscillatory cells (*pacemaker cells*) within the sinoatrial node placed in the upper part of the right atrium. The transmembrane potential propagation and the consequent myocardium depolarization is quite insensitive to the time duration and amplitude of I_s which here have been set to 1 ms and 0.3 $\mathrm{mA \cdot mm^{-2}}$, respectively.

As explained in the Introduction, the transmembrane potential does not propagate along a single heterogeneous medium but rather across a hierarchy of systems whose electrical connection occurs only through selected points. In fact, the electrical signal travels, at a velocity of about 1 m/s, along the internodal pathways and the bundle of Bachmann which are elongated 1D structures. The atrioventricular node is the only electrical conduction between atria and ventricles and there the conduction velocity is only ≈ 0.05 m/s, thus delaying the transmission of ≈ 100 ms before moving beyond. The signal then reaches the bundle of His and speeds up to 2 m/s following the left and right branches which are also 1D filaments. These bundles connect to a very fine 2D network, the Purkinje fibers, in which the signal accelerates to 4 m/s and rapidly reaches the 3D ventricular myocardium where it slows down at < 1 m/s.

All these anatomical structures are explicitly simulated by our electrophysiology model which integrates equations (10) on 1D, 2D or 3D domains depending on the specific heart region and using for each of them the appropriate properties. It is worth mentioning that all these subsystems are two–way coupled among them although only through selected points, the communication nodes, where electrical conduction is allowed. Further details, validations and specific values of the model parameters can be found in [26] where also the numerical scheme used for the integration of the system (10) is thoroughly described.

Here we only mention that the governing equations are solved by a numerical scheme developed in–house to cope with the electrophysiology equations in complex geometries: The domain is split into a 1D graph for the fast conduction bundles, 2D shells for the Purkinje network and an anisotropic 3D medium for atrial and ventricular myocardium which are segmented, respectively, using linear, triangular and tetrahedral elements.

As detailed in [26], all unknowns are defined at the cell center while the equations, written in conservative form, are discretised by second–order accurate finite volume schemes with the transmembrane potential v integrated explicitly in time and the extracellular potential v_{ext} obtained through an iterative GMRES method with restart [47] using the potential at the previous time step as initial guess for the unknown.

Special care is needed to integrate the cellular model (the third of equations (10)) whose state vector $\mathbf{s}$ contains 21 variables for the Courtemanche model of the atria, 20 for the Stewart used in the Purkinje network and 19 for the ten Tusscher–Panfilov model for the ventricular myocardium. Each of them entails the solution of ODEs in time for every spatial cell and those quantifying the ionic fluxes through the cell membrane pores (gating variables) are numerically stiff. Prohibitively small time steps are avoided by integrating analytically the quasi–linear equations for the gating variables (with the transmembrane potential v held constant) and using a time–explicit method for the remaining nonlinear ones. This is known as the Rush–Larsen scheme [48, 49] and its enhanced stability properties allow for a timestep more than one order of magnitude larger than for a standard explicit scheme.

Once the transmembrane potential v_n is known at every cell node, the active muscular tension τ_n^{act} is obtained by the relation [50]

$$\frac{\mathrm{d}\tau_n^{act}}{\mathrm{d}t} = \psi(v_n)[k_\tau v_n - \tau_n^{act}], \tag{14}$$

where k_τ controls the amplitude of the active stress and ψ is a smoothed Heaviside function (increasing monotonically from 0.1, during muscular contraction, to 1, during relaxation), which sets the delay of the active stress with respect to the action potential (see [51] for more details). The active tension at the nodes translates in an active force oriented as the local muscular fiber direction according to:

$$\mathbf{F}_n^{act} = \tau_n^{act} \tilde{l}_n^2 \hat{\mathbf{e}}_f, \tag{15}$$

where $\tilde{l}_n$ is the average length of the mesh edges sharing the node n and $\hat{\mathbf{e}}_f$ the local unit vector aligned along the fibers.

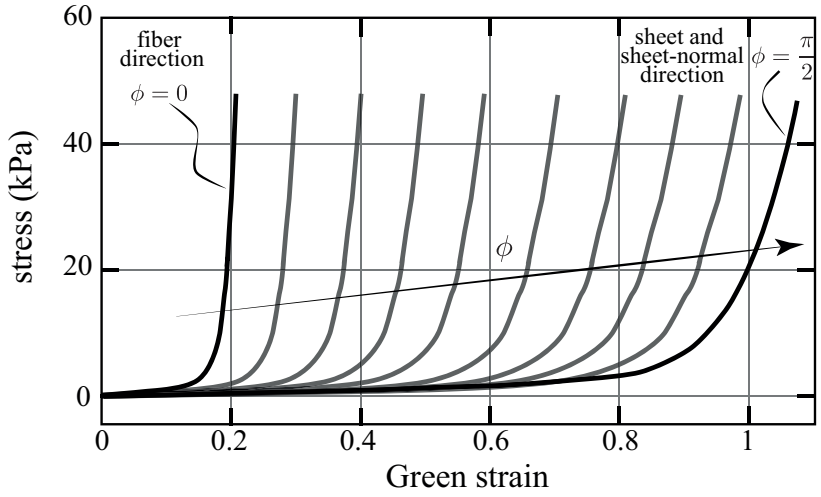

FIG. 6. (a) Hyperelastic and orthotropic constitutive relation as a function of the local inclination in between the mesh edge and the fiber direction. The two limiting cases of edge parallel ($\phi = 0$) and orthogonal ($\phi = \pi/2$) to the local fiber direction are shown by the thicker lines.

C. Structure mechanics

The dynamics of deformable biological tissues is generally tackled by solving the Cauchy–Poisson equation, complemented by appropriate constitutive relations, using finite–element or finite–volume methods. For the present problem however, entailing large time–dependent displacements and deformations, these classical methods imply excessive computational burden and alternative approaches have to be employed. The interaction potential method [52] has proven to be very efficient for these problems [35, 53] and it allows to handle within the same framework three–dimensional tissues, used for the ventricular and atrial myocardium, as well as two–dimensional membranes or shells adopted for valve leaflets, veins and arteries.

The strength of the method lies in its simplicity: the structure is described by triangular (2D) or tetrahedral (3D) elements and the mass is evenly distributed among the nodes which are connected by elastic links. The dynamics of the n–th node obeys the second Newton's law of motion

$$m_n \frac{\mathrm{d}^2 \mathbf{x}_n}{\mathrm{d}t^2} = \mathbf{F}_n^{ext} + \mathbf{F}_n^{int} + \mathbf{F}_n^{act}, \tag{16}$$

with $\mathbf{x}_n$ the node position and on the right hand side external, internal and active forces acting on each mesh vertex.

Note that here external forces are hydrodynamics loads (9) which are non—zero only on the nodes located on wet surfaces, whereas the active tensional force (15) is non–zero only for the nodes belonging to contractile myocardium of ventricles and atria. Internal forces depend on the material constitutive relation and they are specified in the next subsections for 3D and 2D structures. They can also include additional constraints, like incompressibility or surface preservation as shown in [18, 35].

1. 3D myocardium

The 3D structural model starts from the tetrahedral discretization of ventricles and atria which is typically the same mesh used by the electrophysiology solver. Elastic links connect the adjacent nodes of the network and they yield reaction forces when their relative position changes. Although this was originally proposed in the framework of linear elastic materials [54], it can be extended to the case of hyperelastic and anisotropic materials to model the biological tissues with fibers. In fact, these materials are stiffer in the fiber direction ($\hat{\mathbf{e}}_f$) than in the sheet ($\hat{\mathbf{e}}_s$) and sheet–normal ($\hat{\mathbf{e}}_n$) directions and the stiffness increases nonlinearly with the strain. These anisotropic, hyperelastic continua can be described by a Fung–type constitutive relation for which the strain energy density can be written as:

$$W_e = \frac{c}{2}(e^Q - 1), \tag{17}$$

with $Q = \alpha_f \epsilon_{ff}^2 + \alpha_s \epsilon_{ss}^2 + \alpha_n \epsilon_{nn}^2$ being a combination of the Green strain tensor components [55] in the fiber, ϵ_{ff}, sheet, ϵ_{ss}, and sheet–normal ϵ_{nn} directions. The general expression for Q [35, 55], which includes also the cross terms of the

Green strain tensor, has been simplified under the assumption of pure axial loading and, consequently, the non–null second Piola–Kirchhoff stress tensor components in the three directions read $\tau_{ff} = c\alpha_{ff} e^{\alpha_{ff}\epsilon_{ff}^2}\epsilon_{ff}$, $\tau_{ss} = c\alpha_{ss} e^{\alpha_{ss}\epsilon_{ss}^2}\epsilon_{ss}$ and $\tau_{nn} = c\alpha_{nn} e^{\alpha_{nn}\epsilon_{nn}^2}\epsilon_{nn}$. The latter two terms can be taken as equal since it is found experimentally that $\alpha_{nn} = \alpha_{ss}$ [56, 57], implying that the local axial stress of the mesh springs only depends on their inclinations, ϕ, with respect to the local fiber direction. Hence, the local stress within an edge inclined by ϕ with respect to the local fiber direction is computed as

$$\tau_\phi = c\alpha_\phi e^{\alpha_\phi \epsilon_\phi^2}\epsilon_\phi, \tag{18}$$

where $\alpha_\phi = \sqrt{\alpha_{ff}^2 \cos^2\phi + \alpha_{nn}^2 \sin^2\phi}$ (we recall, assuming $\alpha_{nn} = \alpha_{ss}$). The strain ϵ_ϕ is calculated as the spring elongation relative to its instantaneous length, i.e. $\epsilon_\phi = (l - l_0)/l$, where l and l_0 are the actual and the stress–free length of the edge, respectively. As shown in figure 6, the stress increases linearly with the strain for small amplitudes and then grows exponentially for larger deformations. Concerning the alignment with the local fiber orientation, the stiffness is inversely correlated with the angle ϕ thus the force applied to the nodes n and m sharing the link of length $l_{n,m}$ reads:

$$\mathbf{F}_n^{el} = \underbrace{\tau_\phi}_{\text{stress}} \underbrace{\sum_{j=1}^{N_{n,m}} \frac{V_{cj}}{l_{n,m}}}_{\text{tissue cross–section}} \underbrace{\frac{\mathbf{r}_n - \mathbf{r}_m}{l_{n,m}}}_{\text{force direction}}, \qquad \mathbf{F}_n^{el} = -\mathbf{F}_m^{el}, \tag{19}$$

with $\mathbf{r}_n$ ($\mathbf{r}_m$) the position of the node n (m) and V_{cj} the area of the j–th tetrahedron out of the $N_{n,m}$ ones sharing the edge $l_{n,m}$. The parameters of the Fung constitutive relation are set as in [20], so as to reproduce the stress–strain curves in the fiber and cross–fiber direction measured in the ex–vivo experiments.

The mass of the tissue is concentrated on the vertices of the discretising tetrahedra, uniformly distributed and proportional to their volume: given a tissue local density ρ_j, the mass of the j–th element of volume V_j is equally distributed among its four vertices thus the mass of a node, m_n, is

$$m_n = \frac{1}{4}\sum_{j=1}^{N_n} \rho_j V_j, \tag{20}$$

with the summation extended only to the N_n tetrahedra sharing the node n. Here, the tissue density ρ_j is assumed to be uniform within the myocardium and equal to 1.05 g/ml.

2. 2D membranes

Valve leaflets are thin deformable structures which can be modeled as shells and their internal stresses computed using the 2D link network given by surface triangulation [18, 35, 55]. Similarly to the above 3D model, the anisotropic and hyperelastic material properties are accounted for by the same Fung constitutive relation as in (17) and the mass is lumped at the nodes proportionally to the area of the triangles sharing a given vertex [18, 35, 55]. Thus the mass m_n of the n–th node is

$$m_n = \frac{1}{3}\sum_{j=1}^{N_n} \rho_j s_j A_j, \tag{21}$$

where ρ_j and s_j are the local density and tissue thickness, respectively, A_j the area of the triangular element and N_n the number of triangles sharing the n–th node.

Once again internal stresses are computed using equation (18) to account for the local fiber orientation and the forces exerted by the link connecting the nodes n and m is

$$\mathbf{F}_n^{el} = \underbrace{\tau_\phi}_{\text{stress}} \underbrace{s\frac{A_{n,m}^{(1)} + A_{n,m}^{(2)}}{l_{n,m}}}_{\text{tissue cross–section}} \underbrace{\frac{\mathbf{r}_n - \mathbf{r}_m}{l_{n,m}}}_{\text{force direction}}, \qquad \mathbf{F}_m^{el} = -\mathbf{F}_n^{el}, \tag{22}$$

where $\mathbf{r}_n$ ($\mathbf{r}_m$) is the position of the node n (m) and $A_{n,m}^{(1,2)}$ are the areas of the two triangles sharing the edge $l_{n,m}$.

Since the relation (22) accounts only for the in–plane stiffness, an additional bending energy term is added to

provide out–of–plane bending stiffness to the shells and prevent their wrinkling. The out–of–plane deformation of two adjacent triangles sharing an edge is then associated with an elastic reaction of a bending spring, whose energy involves four adjacent nodes [35]. Considering a surface with non–zero initial curvature in the stress–free configuration, the discretized bending energy can be written as [58]

$$W_b = k_b[1 - \cos(\theta - \theta_0)], \tag{23}$$

where θ is the angle between the normals of adjacent triangular faces of the tessellated surface, and θ_0 is the neutral angle of the stress–free configuration. The bending constant is equal to $k_b = 2B/\sqrt{3}$ [35, 59], with $B = c\alpha_\phi s^3/[12(1-\nu_m^2)]$ the bending modulus of a planar structure, where s is the tissue thickness, $c\alpha_\phi$ is the equivalent Young modulus in the limit of small strain (which depends on the Fung tissue properties) and $\nu_m = 0.5$ is the Poisson ratio of the material. The corresponding bending nodal forces, $\mathbf{F}_n^{be}$ can be then obtained by taking the gradient of the bending potential (23) as detailed in [35].

The total internal force of these 2D shells at a given node is thus given by

$$\mathbf{F}_n^{int} = \mathbf{F}_n^{el} + \mathbf{F}_n^{be}, \tag{24}$$

to be used in equation (16) to compute the time–dependent dynamics.

During the heart beat cardiac valves open and close alternatively and their leaflets are pushed against each other, during the closing phase, to seal the valve. In order to prevent the structures from piercing each other during the approaching phase, the contact model developed in [16] has been used. It consists of tagging, at each time step, the cells of the fluid domain occupied by a structure node with an integer number corresponding to the body to which the node belongs (untagged cells are entirely occupied by the fluid). Whenever a node of a moving body enters a tagged cell, a contact is detected and the two nodes belonging to different bodies are forced to move with the average of their incoming velocity, so that they can drift in space without compenetration. In contrast, if the local forces pull them apart, the structures can freely recede without any constraint. Of course, as two bodies approach, and the gap between them contains less than ≈ 3–4 gridpoints, the spatial resolution becomes insufficient to capture the flow and a subgrid model should be used to estimate the hydrodynamic loads generated by their relative motion. Among many, one possibility consists of solving the Stokes or the lubrication equations in the gap to compute the overpressure (underpressure) induced by the approaching (receding) phase; this avoids incorrect contact dinamics when the gap between the tissues becomes too narrow to be resolved by the grid spacing [60]. We wish to stress that this, and similar models available from the literature, entail a non–negligible computational overhead and reduce the numerical stability of the computational model: we are currently working on these issues before employing this model for our cardiac simulations.

3. Model coupling and computational implementations

The description of the three main models makes it immediately evident that none of them is standalone and each one relies on the results of the others as input: in fact, the integration of equation (16), from which the actual tissue configuration is obtained, needs the hydrodynamic loads and the active myocardium tension given, respectively, by flow and electrophysiology solvers. On the other hand, the system (1) can only be tackled once the fluid domain is known which is determined by the structure model. Finally, equations (10) depend on the structure solver not only for the domain configuration but also because the conductivity tensors $\hat{M}^{ext}$ and $\hat{M}^{int}$ might be altered by the local strain [61].

On account of the complex physical interconnection it is not clear whether these systems should be advanced in time simultaneously or whether they could be solved sequentially and, in the latter case, in which order. The former strategy, referred to as strong–coupling, considers all models as a unique dynamical system whose solution is stable although computationally expensive. In contrast, the alternative method, the loose–coupling, yields relatively inexpensive schemes at the price of more unstable solutions which require smaller time steps.

The most advantageous approach, in terms of time–to–solution, depends on the problem and on the specific parameters therefore both, strong– and loose–coupling, have been implemented in the present model [18]. The first is based on a predictor–corrector two–step Adams–Bashforth scheme with the three solvers iterated within each time step (typically 2–3 times) until the maximum relative error computed on the position and velocity of the structural nodes decreases below a prescribed threshold (usually 10^{-4}). In the loose–coupling method, fluid and electrophysiology are solved first, using the structure at the previous time step, and the generated hydrodynamic and active loads are used to evolve the new structure.

For the application presented in this paper [18] have shown that the time step is fixed by the fast electrophysiology dynamics and the high frequencies of the stiff myocardium during systole; since the limitation comes from physical

rather than from numerical constrains, a loose–coupling strategy has shown to provide stability and computational time savings of the order of 50-–70% while giving the same results as the strong coupling.

Accordingly, for all results shown in this paper, a loose–coupling approach has been employed and a dynamic time step with a constant Courant number CFL = 0.2 has yielded a $\Delta t \approx 2\mu s$ throughout the simulations.

Before showing the results, it is worthwhile to summarize some details about the computational cost of the model since, given the huge undertaking, without an efficient implementation it would be impossible to run the simulation campaigns needed for parametric studies. In fact, the model was originally parallelized using MPI directives and run on standard CPU clusters: the reference configuration with a grid of 211 Mnodes could use a maximum of 144 CPUs before the parallel performance was too degraded and, on the Cartesius cluster of SURFsara (https://www.surfsara.nl/), it required ≈ 2 s of wallclock time per time step thus, with a time step $\Delta t \approx 2\mu s$, the integration of a heartbeat could be completed in not less than 12 days. It must be mentioned that for each case the first heartbeat is discarded since it accommodates the initial transient and the pretensioning of all tissues while an order of 5 additional statistically steady heartbeats are computed in order to obtain phase–averaged statistics of the pulsatile flow. With the above numbers, each simulation needed about 2 months to be completed and these numbers were clearly incompatible both, with the clinical practice and extensive parametric studies.

An important breakthrough for this model has been its porting to GPUs whose architecture turned out particularly beneficial for the present software: using 8 NVIDIA A100 GPUs, the same above simulation could be run in ≈ 0.07 s per time step and ≈ 10 hours per heartbeat [27] thus allowing a complete simulation in 2.5 days.

This impressive speedup has allowed the use of the present model for large simulation campaigns in which input data and configurations are systematically varied to reproduce a cohort of virtual patients as would be done in clinical trials. In the next section, we will show first the results obtained for a healthy configuration and then some pathologic cases with myocardial infarction in which, by changing the position of the necrotic scar, the effect of the disorder on the overall pumping function is discussed.

IV. RESULTS AND DISCUSSIONS

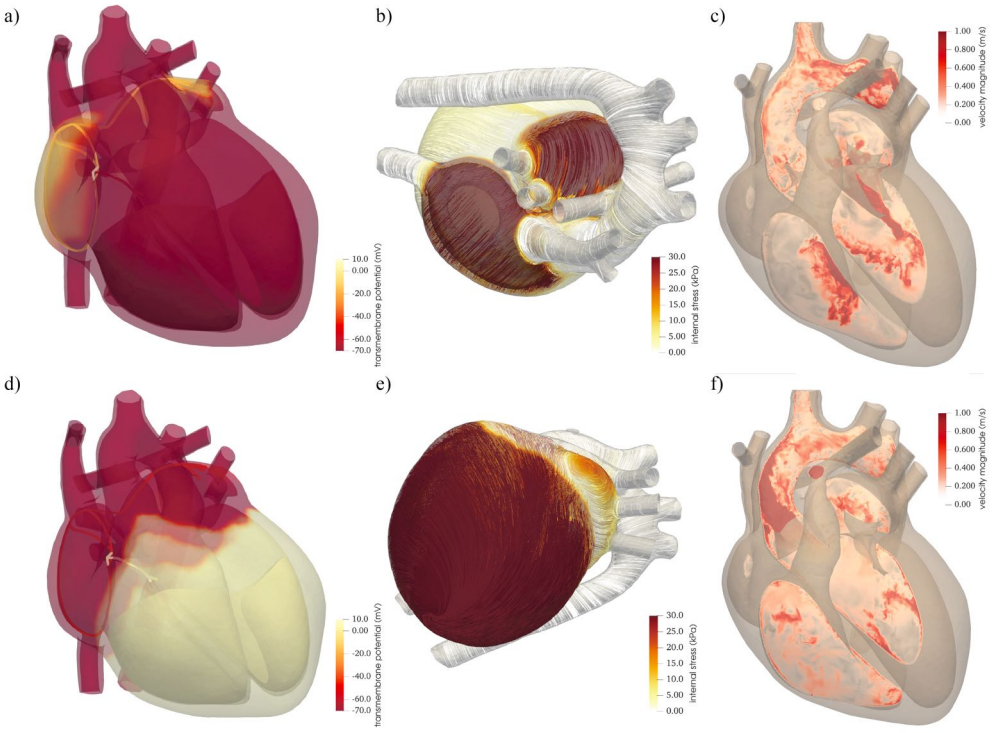

FIG. 7. Perspective views, for the healthy configuration, of instantaneous distributions of activation potential (a) and (d), internal tissue stress (b) and (e) and blood velocity magnitude on a plane cutting the left ventricle (c) and (f). a), b) and c) are for late diastole, d) e) and f) for peak systole.

A. Physiologic conditions

In order to better identify the effects of myocardial infarction, we will present first some data obtained from the model run with nominal healthy parameters: this configuration will be regarded as a reference and any change produced by the disorder will be identified by comparison.

The main results obtained for healthy conditions are discussed in [20] and in figure 7 electrophysiology, tissue loads and hemodynamics are reported at ventricular diastole and systole. Note that, owing to the complex three dimensional structure of the heart, a single planar section cannot properly visualize the flow in the left and right side and, in this paper, the former has been privileged.

One important result of the model is the time evolution over a heartbeat of the left ventricular blood pressure, of its volume and of the aortic blood pressure (figure 8) since these quantities are widely used in clinical practice and have relevant diagnostic value. In fact, the peak of the aortic pressure is the systolic (maximum) value while the baseline is the diastolic (minimum) value which, in any routine medical check are immediately acquired by the physician to make an evaluation.

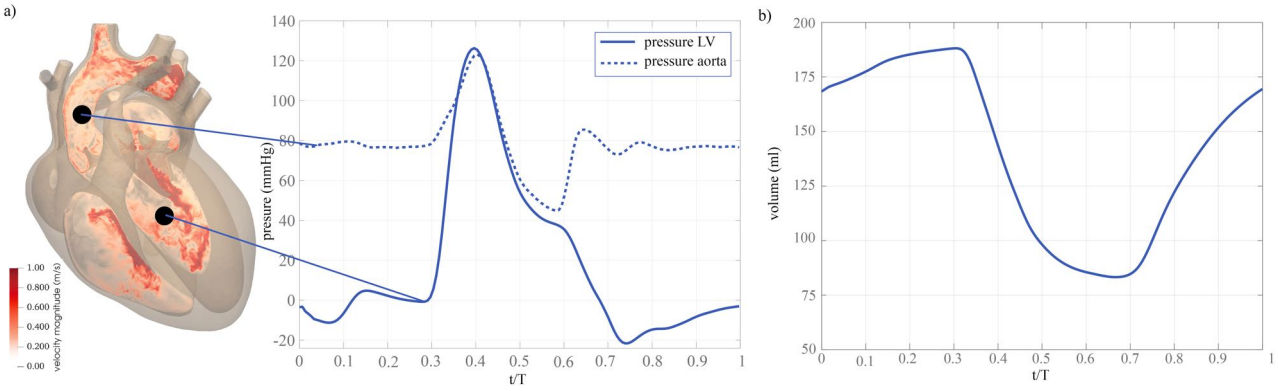

FIG. 8. a) Time evolution, during a complete heartbeat, of left ventricle (———) and aortic (– – – –) blood pressure. b) Time evolution of the left ventricle volume.

The time evolution of the left ventricle volume, usually estimated by simple ultrasound scan imaging, yields the ejection fraction $EF\% = (V_M - V_m)/V_M$, with V_M and V_m the maximum and minimum left ventricular volume over an heart beat. The EF gives a concise assessment of the cardiac pumping efficiency: values in the range $\geq 50\%$ are normal, 50%–30% are moderately to severely reduced while $\leq 30\%$ are life threatening. Finally, the ejection fraction multiplied by the heart rate gives the cardiac output (CO, usually in liter per minute) which is the blood flow rate pumped in the circulations. Additional information can be obtained from the crossings of aortic and ventricular blood pressure that mark the opening and closing of the aortic valve or the shape of the waveforms which indicates the relative duration of systolic and diastolic phases. The values obtained from the present model, run under nominal values of the parameters, are 130 mmHg/80 mmHg (17290 Pa/10640 Pa) for systolic/diastolic pressure, $EF\% = 55.7$ and $CO = 7.3$ l/min which are typical figures for a healthy adult male.

B. Infarcted myocardium

The heart has very limited anaerobic capacity and oxygen shortage, even of just a few minutes, can result in permanent damage. In fact, myocytes extract up to 80% of the available oxygen from the blood, unlike skeletal muscles which use only 30–40% of it [63], therefore they depend on a continuous supply of oxygenated blood from the coronary circulation. The latter starts from the left and right coronary arteries, originating from two Valsalva sinuses of the aortic root, and by successive branchings feeds a superfine network of capillaries reaching all myocardial cells. If a clot ends up in one coronary artery and it gets stuck in one of the branches, all the downstream flow is decreased of completely blocked and the perfused tissue is impaired. Indeed some residual tissue oxygenation is still possible thanks to retrograde secondary perfusion from the surrounding capillary bed, therefore the final outcome of an ischemic event shows huge variability ranging from complete recovery to death. If the clot is eliminated (usually by drug dissolution) within the first few minutes the event is reversible and myocardial function is restored partially or totally. In contrast, if oxygen shortage lasts beyond a hour the interested region necrotizes becoming a scar with altered elastomechanic and electrophysiologic properties [64].

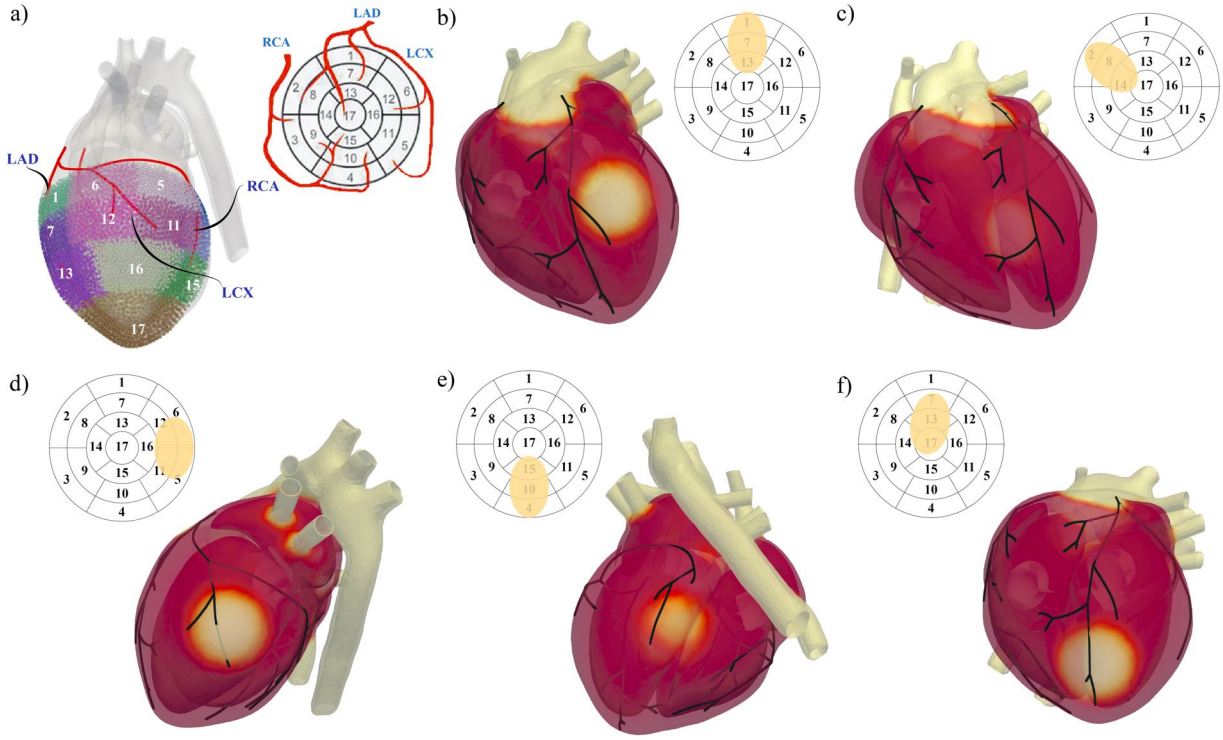

FIG. 9. a) Left ventricle segmentation according to [62]. b)–f) show the position of our 'minimal' infarction and the affected LV segments; b) Anterior infarction (segments 1–7–13); c) Septal (2–8–14); d) Lateral (5–6–11–12); e) Inferior (4–10–15); f) Apical–Anterior (1–7–13–17).

Among the factors determining the damage, there are the area of the ischemic tissue, the depth across the thickness and the position in the heart. The left ventricle is by far the part most damaged by heart attacks and for this reason cardiologists have segmented its myocadium into 17 sectors and cataloged the affected ones for the most common ischemic events [62]. In figure 9 we show the map of the segmented regions together with the location of the five ischemic events considered in this study.

Concerning the infarct in the myocardium, for all cases, we have considered a 'minimal infarction' consisting of a circular scar region centered at $\mathbf{x}_i$ of radius $\sigma_i = 2$ cm of partially necrotized tissue which is surrounded by an annular border zone of size 1 cm [65]; the ischemic endocardium is about 9% of the total left ventricle wet surface. Although in reality the necrosis can affect different thickness depths of the myocardium, here we have assumed that the scar always extended from the epicardium to the endocardium (transmural ischemia). Finally, within the infarcted area a shape function $f(\mathbf{x}) = \exp[-((\mathbf{x}-\mathbf{x}_i)/\sigma_i)^8]$ modulates the tissue stiffness with the factor $1+f(\mathbf{x})$ while the electrophysiology conductivity and the active tension with the factor $1-f(\mathbf{x})$. In this way the necrotic scar is twice stiffer than the corresponding healthy tissue and it has no electric conduction and active contraction. Furthermore the shape function $f(\mathbf{x})$ smoothly connects the properties of the impaired and healthy tissue thus mimicking the perinfarct region with some residual functionality [66].

Figure 10 shows a perspective view of the tissue stress distribution for the various cases at $t/T = 0.44$ which is around peak systole; it appears that generally, given the limited extent of the impaired region, ventricle contraction is mostly preserved, the case of septal infarction being the only exception. The distribution of the activation potential (figure 11) gives similar information and clarifies the reason for the latter atypical behavior. In fact, for all cases but the septal infarction, although the scar does not conduct the electrical signal, the surrounding tissue can make up for it thus preventing the blocking or delaying of ventricle depolarisation. In contrast, within the interventricular septum is embedded the bundle of His which branches into left and right bundles (figure 1a), the elongated fast conduction fibers, bringing the activation potential to the Purkinje network of left and right ventricles, respectively. The ischemic scar of our septal infarction, located across segments 8 and 14, impairs a tract of the left bundle branch thus cutting the electrical connection between the bundle of His and the left Purkinje network. As a consequence, the left ventricle contracts only when the depolarisation wave from the right ventricle propagates along the myocardium (see [20]) where the conduction velocity is only ≈ 0.5 m/s rather than ≈ 4 m/s of the Purkinje fibers.

This dynamics is well evidenced by the pressure profiles of figure 12 showing that, for the septal infarction, the left

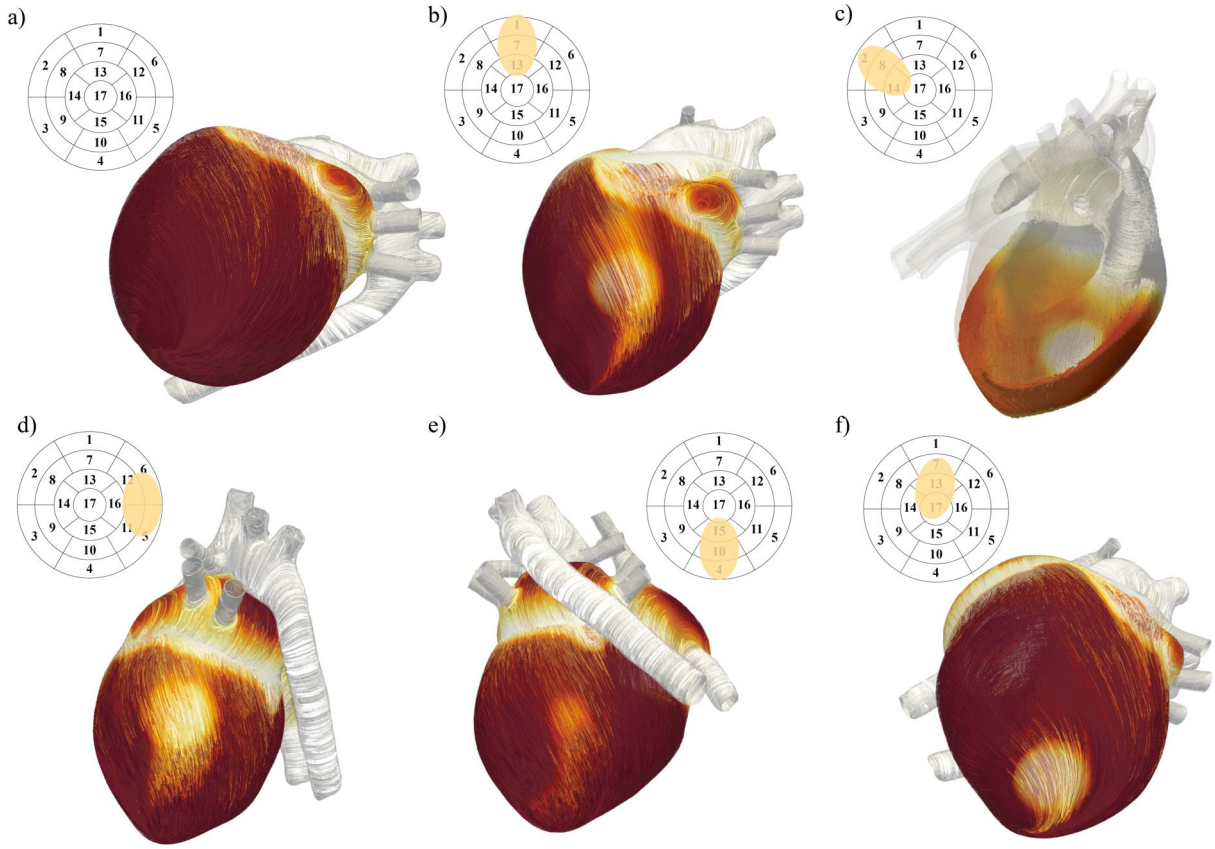

FIG. 10. Internal stresses of the myocardium at peak systole ($t/T = 0.44$): a) healthy case; b)–f) infarcted hearts as in figure 9. The stress level is color coded as in figure 7e.

	Healthy	Anterior	Septal	Lateral	Inferior	Apical–Anterior
Impaired Sectors	–	1-7-13	2-8-14	5-6-11-12	4-10-15	1-7-13-17
Max LV pressure (mmHg)	128.0	117.1	108.9	115.6	118.0	118.2
Ejection fraction (EF)	55.7	52.0	49.9	50.5	52.0	52.6
Cardiac Output (l/min)	7.3	6.8	6.1	6.6	6.8	6.9

TABLE II. Efficiency indicators for the heart pumping function in the various simulated cases.

ventricle systole is delayed by ≈ 150 ms with a peak pressure and a volume contraction which are the smallest among all cases. In fact, the contraction asynchrony of left and right ventricles destroys their synergistic action and decreases the overall pumping efficiency of the heart as shown by the data of Table II. Figure 13 shows the hemodynamics on a plane cutting the left ventricle at $t/T = 0.44$, which is the peak systole for the healthy configuration as confirmed by the strong aortic jet in panel a). On the other hand, at the same time, the heart with the septal infarction (figure 13b) is only at the beginning of its contraction since the depolarisation wave has not reached the whole muscular tissue. When, at $t/T = 0.55$, the ventricle fully depolaraises (figure 13c) the contraction is weaker and the aortic jet less intense than in the reference case.

The loss of electrical connection between the bundle of His and the left Purkinje network is known as left bundle branch block and it can be due to different causes like cardiomyopathies and endocarditis although coronary artery diseases are among the most common [67].

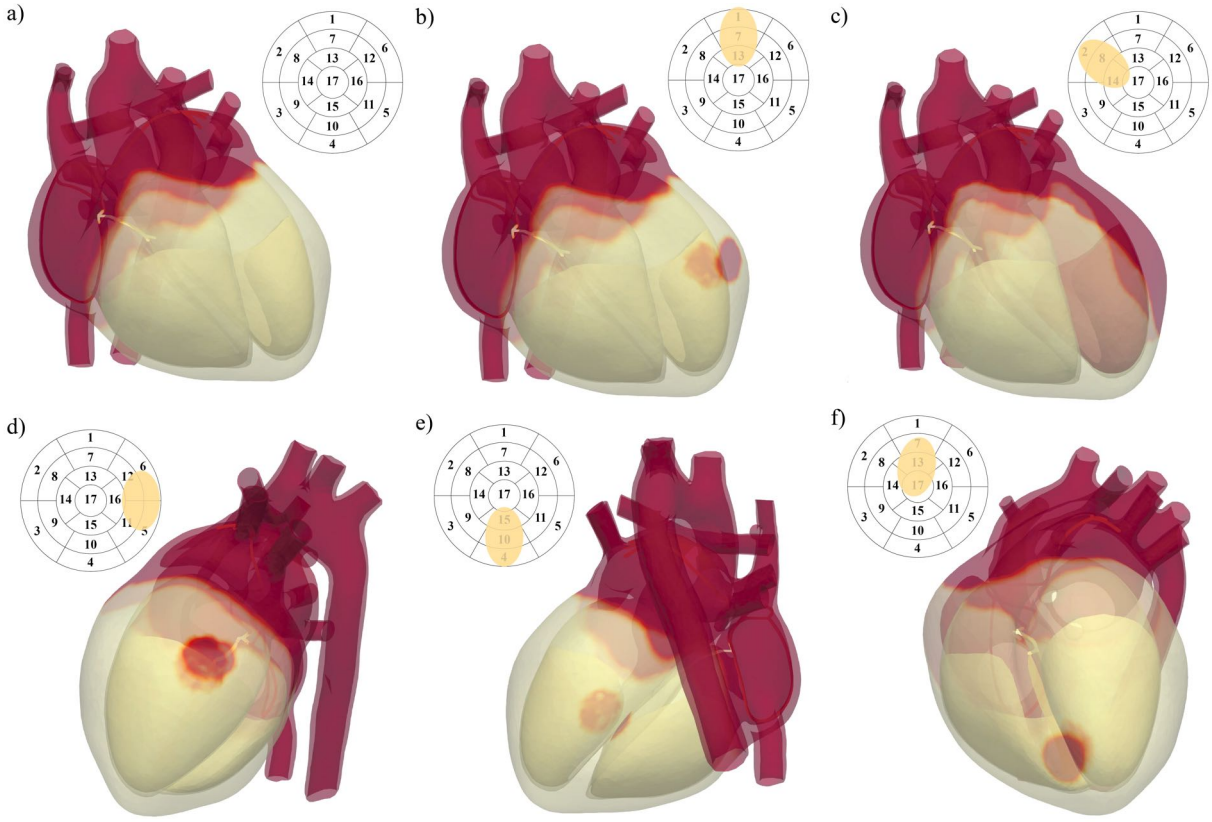

FIG. 11. Activation potential of the hearts at peak systole ($t/T = 0.44$): a) healthy case; b)–f) infarcted hearts as in figure 9. The stress level is color coded as in figure 7d.

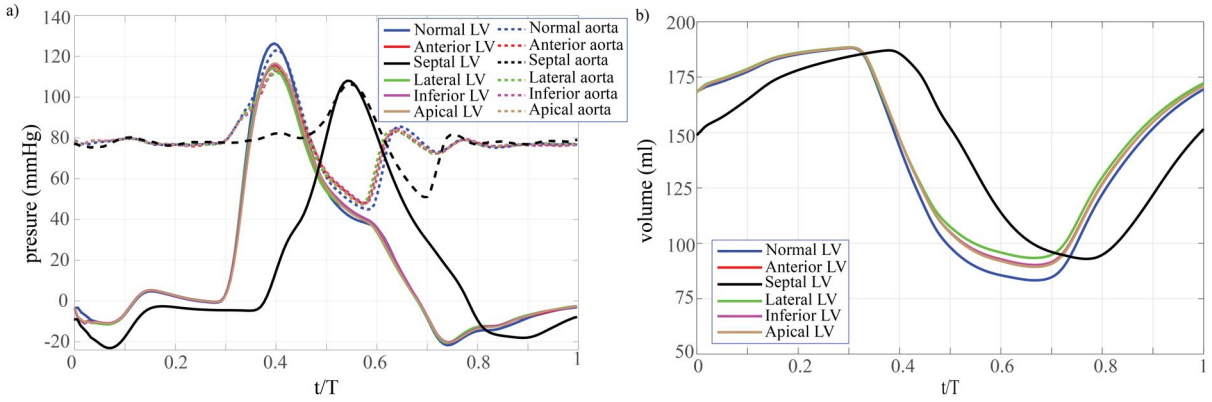

FIG. 12. a) Time evolution, during a complete heartbeat, of left ventricle and aortic blood pressure: comparison between healthy and infarcted hearts. b) Time evolution of the left ventricle volume.

V. CONCLUSIONS

In this paper we have illustrated and described a computational tool aimed at reproducing with high fidelity the full dynamics of the human heart. To achieve this goal three different models have been developed to emulate the elastomechanics of active and passive heart tissues, the electrophysiology systems including its hierarchical structures and the blood hemodynamics.

A complex and important aspect is the multi–way coupling of all these systems which entail sophisticated numerical techniques for their concurrent integration. The resulting model reproduces with high fidelity and predictive capabilities the dynamics of the heart, however at the price of huge computational costs which, on common CPU clusters,

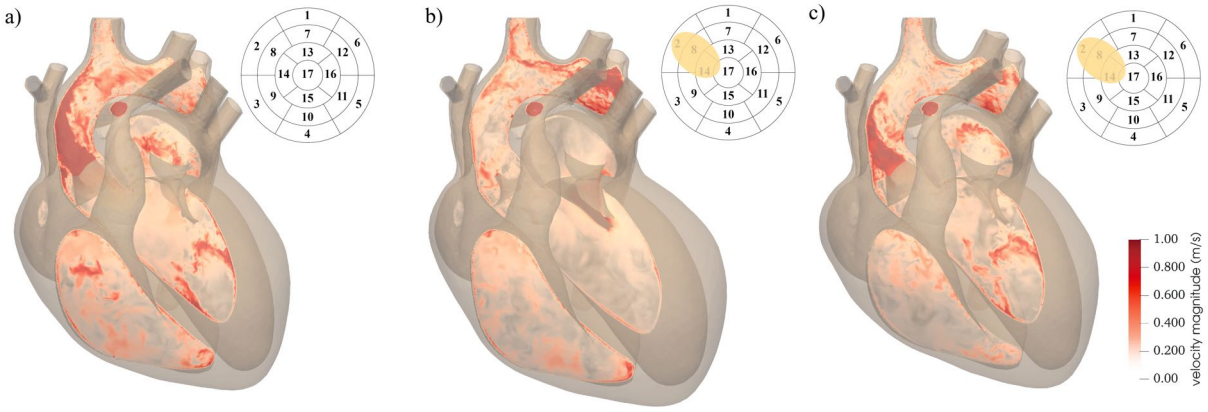

FIG. 13. Comparison of the LV hemodynamics at $t/T = 0.44$ a) healthy case (peak systole); b) septal infarction. c) The same as b) but at $t/T = 0.55$ which is the peak systole for the case of septal infarction.

would allow only flagship simulations. Since the long term aim of this research is to make of this model a useful tool for clinical research, an effort has been made to port all the software on the latest GPU architectures [27] and this has reduced the time to solution from months to days which makes possible clinical applications.

Some illustrative results have been produced for a reference healthy configuration and for several cases of myocardial infarction: it has been shown that not only the model yields the physiological parameters when run in nominal conditions but it can also reproduce subtle details of cardiovascular disorders thanks to its detailed multi–physics modelling.

Before concluding this paper we wish to stress that, even if the present results confirm that the model behaves as clinicians would expect, still there are many aspects to be improved. The electrophysiology modeling should account for the modifications on the ionic currents and on the action potential duration/restitution induced by the ischemia, which are known to generate abnormal depolarization patterns (spiral and scroll waves) and eventually induce cardiac arrhythmia [68, 69]. Accounting for such abnormalities would allow the digital heart to predict the arrhythmic potential and the risk of ventricular tachycardia along with the corresponding impaired hemodynamics as a function of the location/shape of the ischemic region and the cardiac anatomy.

As a last main point we mention the heart geometrical parameters and all tissue properties which, given the scattered values, should be analyzed by uncertainty quantification techniques. This implies that rather than running single deterministic simulations, large simulation campaigns should be performed with the results presented in terms of probability distributions. This approach has already been used for small portions of the heart [70] and is currently being pursued for the whole organ in an ongoing investigation.

ACKNOWLEDGMENTS

This project has received funding from the European Research Council (ERC) under the European Union's Horizon Europe research and innovation programme (Grant agreement 101039657, CARDIOTRIALS to FV). CINECA is gratefully acknowledged for the access to high performance computing resources under the computational grant IsB23-CaRdiopT. R.V. wishes to thank the financial support of Italian Ministry of Education under the contract n. 2017A889FP

[1] E. Popa, M. van Hilten, E. Oosterkamp, and M. Boogardt, The use of digital twins in healthcare: socio-ethical benefits and socio-ethical risks, Life Sciences, Society and Policy **17** (2021).
[2] F. Italianer and *et al.*, European heart network: Annual report 2020, https://ehnheart.org/annual-reports.html (2021).
[3] J. Womersley, *An elastic tube theory of pulse transmission and oscillatory flow in mammalian arteries*, Tech. Rep. (Air Res. and Dev. Command, US Air Force, Ohio, US, 1957).
[4] C. S. Peskin, Flow patterns around heart valves: a numerical method, Journal of computational physics **10**, 252 (1972).
[5] F. Sotiropoulos, T. Le, and A. Gilmanov, Fluid mechanics of heart valves and their replacements, Annual Review of Fluid Mechanics **48**, 259–283 (2016).

[6] K. Jan, Distribution of myocardial stress and its influence on coronary blood flow, Journal of Biomechanics **18**, 815 (1985).

[7] e. a. Gijsen FJH, Van de Vosse FN, The influence of the non-newtonian properties of blood on the flow in large arteries: Steady flow fields in carotid bifurcation model, Journal of Biomechanics **32**, 601 (1999).

[8] G. Holzapfel and R. Ogden, Constitutive modelling of passive myocardium: a structurally based framework for material characterization, Phylosofical Transactions of Royal Society **367**, 3445 (2009).

[9] C. M. Augustin, M. A. Gsell, E. Karabelas, E. Willemen, F. W. Prinzen, J. Lumens, E. J. Vigmond, and G. Plank, A computationally efficient physiologically comprehensive 3d–0d closed-loop model of the heart and circulation, Computer methods in applied mechanics and engineering **386**, 114092 (2021).

[10] L. Dedè, F. Menghini, and A. Quarteroni, Computational fluid dynamics of blood flow in an idealized left human heart, International journal for numerical methods in biomedical engineering **37**, e3287 (2021).

[11] A. Santiago, J. Aguado-Sierra, M. Zavala-Akè, R. Doste-Beltran, S. Gómez, R. Arís, J. Cajas, and M. Vázquez, Fully coupled fluid–electro–mechanical model of the human heart for supercomputers, International Journal of Numerical Methods for Biomedical Engineering **34**, e3140 (2018).

[12] J. A. Brown, J. H. Lee, M. A. Smith, D. R. Wells, A. Barrett, C. Puelz, J. P. Vavalle, and B. E. Griffith, Patient–specific immersed finite element–difference model of transcatheter aortic valve replacement, Annals of biomedical engineering **51**, 103 (2023).

[13] M. Fedele, R. Piersanti, F. Regazzoni, M. Salvador, P. C. Africa, M. Bucelli, A. Zingaro, A. Quarteroni, *et al.*, A comprehensive and biophysically detailed computational model of the whole human heart electromechanics, Computer Methods in Applied Mechanics and Engineering **410**, 115983 (2023).

[14] R. Verzicco, Electro–fluid–mechanics of the heart, Journal of Fluid Mechanics **941**, P1 (2022).

[15] V. Meschini, M. De Tullio, G. Querzoli, and R. Verzicco, Flow structure in healthy and pathological left ventricles with natural and prosthetic mitral valves, Journal of fluid mechanics **834**, 271 (2018).

[16] V. Meschini, F. Viola, and R. Verzicco, Modeling mitral valve stenosis: A parametric study on the stenosis severity level, Journal of biomechanics (2019).

[17] F. Viola, E. Jermyn, J. Warnock, G. Querzoli, and R. Verzicco, Left ventricular hemodynamics with an implanted assist device: An in vitro fluid dynamics study, Annals of biomedical engineering , 1 (2019).

[18] F. Viola, V. Meschini, and R. Verzicco, Fluid–structure-electrophysiology interaction (fsei) in the left-heart: A multi-way coupled computational model, European Journal of Mechanics-B/Fluids **79**, 212 (2020).

[19] M. Strocchi, C. Augustin, M. Gsell, E. Karabelas, A. Neic, K. Gillette, O. Razeghi, A. Prassl, E. Vigmond, J. Behar, J. Gould, B. Sidhu, C. Rinaldi, M. Bishop, G. Plank, and S. Niederer, A publicly available virtual cohort of four–chamber heart meshes for cardiac electro–mechanics simulations, PLoS ONE **15(6)**, e0235145 (2020).

[20] F. Viola, G. Del Corso, R. J. De Paulis, and R. Verzicco, Gpu accelerated digital twins of the human heart open new routes for cardiovascular research, Scientific Reports **13**, 8230 (2023).

[21] F. Torrent-Guasp, G. Buckberg, C. Clemente, J. Cox, H. Coghlan, and M. Gharib, The structure and function of the helical heart and its buttress wrapping. i. the normal macroscopic structure of the heart, Seminars in thoracic and cardiovascular surgery **13(4)**, 301 (2001).

[22] R. Verzicco, Immersed boundary methods: Historical perspective and future outlook, Annual Review of Fluid Mechanics **55**, 129 (2023).

[23] N. Westerhof, J.-W. Lankhaar, and B. E. Westerhof, The arterial windkessel, Medical & biological engineering & computing **47**, 131 (2009).

[24] M. S. Olufsen, C. S. Peskin, W. Y. Kim, E. M. Pedersen, A. Nadim, and J. Larsen, Numerical simulation and experimental validation of blood flow in arteries with structured-tree outflow conditions, Annals of biomedical engineering **28**, 1281 (2000).

[25] U. Morbiducci, D. Gallo, D. Massai, F. Consolo, R. Ponzini, L. Antiga, C. Bignardi, M. A. Deriu, and A. Redaelli, Outflow conditions for image-based hemodynamic models of the carotid bifurcation: implications for indicators of abnormal flow, Journal of biomechanical engineering **132** (2010).

[26] G. Del Corso, R. Verzicco, and F. Viola, A fast computational model for the electrophysiology of the whole human heart, Journal of Computational Physics **457**, 111084 (2022).

[27] F. Viola, V. Spandan, V. Meschini, J. Romero, M. Fatica, M. de Tullio, and R. Verzicco, Fsei–gpu: Gpu accelerated simulations of the fluid–structure–electrophysiology interaction in the left heart, Computer Physics Communications **273**, 108248 (2022).

[28] D. Katritsis, L. Kaiktsis, A. Chaniotis, J. Pantos, E. P. Efstathopoulos, and V. Marmarelis, Wall shear stress: theoretical considerations and methods of measurement, Progress in cardiovascular diseases **49**, 307 (2007).

[29] F. De Vita, M. D. de Tullio, and R. Verzicco, Numerical simulation of the non-newtonian blood flow through a mechanical aortic valve, Theoretical and Computational Fluid Dynamics **30(1)**, 129 (2016).

[30] M. Rai and P. Moin, Direct simulations of turbulent flow using finite-difference schemes, in *27th Aerospace Sciences Meeting* (1991) p. 369.

[31] R. Verzicco and P. Orlandi, A finite-difference scheme for three-dimensional incompressible flows in cylindrical coordinates, Journal of Computational Physics **123**, 402 (1996).

[32] E. P. van der Poel, R. Ostilla-Mónico, J. Donners, and R. Verzicco, A pencil distributed finite difference code for strongly turbulent wall-bounded flows, Computers & Fluids **116**, 10 (2015).

[33] M. Uhlmann, An immersed boundary method with direct forcing for the simulation of particulate flows, Journal of Computational Physics **209**, 448 (2005).

[34] M. Vanella and E. Balaras, A moving–least–squares reconstruction for embedded–boundary formulations, Journal of Com-

putational Physics **228(18)**, 6617 (2009).
[35] M. D. De Tullio and Pascazio, A moving-least-squares immersed boundary method for simulating the fluid-structure interaction of elastic bodies with arbitrary thickness, to appear in Journal of Computational Physics (2016).
[36] V. Spandan, D. Lohse, M. D. de Tullio, and R. Verzicco, A fast moving least squares approximation with adaptive lagrangian mesh refinement for large scale immersed boundary simulations, Journal of computational physics **375**, 228 (2018).
[37] M. Beeson, Triangle tiling i: the tile is similar to abc or has a right angle, arXiv preprint arXiv:1206.2231 (2012).
[38] M. Courtemanche, R. J. Ramirez, and S. Nattel, Ionic mechanisms underlying human atrial action potential properties: insights from a mathematical model, American Journal of Physiology-Heart and Circulatory Physiology **275**, H301 (1998).
[39] P. Stewart, O. V. Aslanidi, D. Noble, P. J. Noble, M. R. Boyett, and H. Zhang, Mathematical models of the electrical action potential of purkinje fibre cells, Philosophical Transactions of the Royal Society A: Mathematical, Physical and Engineering Sciences **367**, 2225 (2009).
[40] K. Ten Tusscher and A. Panfilov, Cell model for efficient simulation of wave propagation in human ventricular tissue under normal and pathological conditions, Physics in Medicine & Biology **51**, 6141 (2006).
[41] S. A. Niederer, J. Lumens, and N. A. Trayanova, Computational models in cardiology, Nature Reviews Cardiology **16**, 100 (2019).
[42] H. Sutanto and J. Heijman, Integrative computational modeling of cardiomyocyte calcium handling and cardiac arrhythmias: Current status and future challenges, Cells **11** (2022).
[43] B. Nadal-Ginard, J. Kajstura, A. Leri, and P. Anversa, Myocyte death, growth, and regeneration in cardiac hypertrophy and failure, Circulation Research **92**, 139 (2003).
[44] L. Tung, *A bi-domain model for describing ischemic myocardial dc potentials.*, Ph.D. thesis, Massachusetts Institute of Technology (1978).
[45] R. H. Clayton and A. V. Panfilov, A guide to modelling cardiac electrical activity in anatomically detailed ventricles, Progress in biophysics and molecular biology **96**, 19 (2008).
[46] J. Sundnes, G. T. Lines, X. Cai, B. F. Nielsen, K.-A. Mardal, and A. Tveito, *Computing the electrical activity in the heart*, Vol. 1 (Springer Science & Business Media, 2007).
[47] L. N. Trefethen and D. Bau III, *Numerical linear algebra*, Vol. 50 (Siam, 1997).
[48] S. Rush and H. Larsen, A practical algorithm for solving dynamic membrane equations, IEEE Transactions on Biomedical Engineering , 389 (1978).
[49] M. E. Marsh, S. T. Ziaratgahi, and R. J. Spiteri, The secrets to the success of the rush–larsen method and its generalizations, IEEE transactions on biomedical engineering **59**, 2506 (2012).
[50] M. P. Nash and A. V. Panfilov, Electromechanical model of excitable tissue to study reentrant cardiac arrhythmias, Progress in biophysics and molecular biology **85**, 501 (2004).
[51] S. Göktepe and E. Kuhl, Electromechanics of the heart: a unified approach to the strongly coupled excitation–contraction problem, Computational Mechanics **45**, 227 (2010).
[52] D. A. Fedosov, B. Caswell, and G. E. Karniadakis, Systematic coarse-graining of spectrin-level red blood cell models, Computer Methods in Applied Mechanics and Engineering **199**, 1937 (2010).
[53] V. Spandan, V. Meschini, R. Ostilla-Mónico, D. Lohse, G. Querzoli, M. D. de Tullio, and R. Verzicco, A parallel interaction potential approach coupled with the immersed boundary method for fully resolved simulations of deformable interfaces and membranes, Journal of computational physics **348**, 567 (2017).
[54] A. V. Gelder, Approximate simulation of elastic membranes by triangulated spring meshes, Journal of graphics tools **3**, 21 (1998).
[55] P. E. Hammer, M. S. Sacks, J. Pedro, and R. D. Howe, Mass-spring model for simulation of heart valve tissue mechanical behavior, Annals of biomedical engineering **39**, 1668 (2011).
[56] K. D. Costa, P. J. Hunter, J. Wayne, L. Waldman, J. Guccione, and A. D. McCulloch, A three-dimensional finite element method for large elastic deformations of ventricular myocardium: Ii prolate spheroidal coordinates, Journal of Biomechanical Engineering **118**, 464 (1996).
[57] T. Usyk, R. Mazhari, and A. McCulloch, Effect of laminar orthotropic myofiber architecture on regional stress and strain in the canine left ventricle, Journal of elasticity and the physical science of solids **61**, 143 (2000).
[58] Y. Kantor and D. R. Nelson, Phase transitions in flexible polymeric surfaces, Physical Review A **36**, 4020 (1987).
[59] J. Li, M. Dao, C. Lim, and S. Suresh, Spectrin-level modeling of the cytoskeleton and optical tweezers stretching of the erythrocyte, Biophysical journal **88**, 3707 (2005).
[60] R. Verzicco and G. Querzoli, On the collision of a rigid sphere with a deformable membrane in a viscous fluid, Journal of fluid mechanics **914**, A19 (2021).
[61] A. Loppini, A. Gizzi, R. Ruiz-Baier, C. Cherubini, F. Fenton, and S. Filippi, Competing mechanisms of stress–assisted diffusivity and stretch–activated currents in cardiac electromechanics, Frontiers in Physiology **9**, 1714 (2018).
[62] M. Cerqueira, N. Weissman, V. Dilsizian, A. Jacobs, S. Kaul, W. Laskey, D. Pennell, J. Rumberger, T. Ryan, and M. Verani, Standardized myocardial segmentation and nomenclature for tomographic imaging of the heart a statement for healthcare professionals from the cardiac imaging committee of the council on clinical cardiology of the american heart association, Circulation **105(4)**, 539 (2002).
[63] A. Goodwill, G. Dick, A. Kiel, , and J. Tune, Regulation of coronary blood flow, Comprehensive Physiology **7(2)**, 321 (2018).
[64] N. Sperelakis, *Physiology and Pathophysiology of the Heart* (Springer Science + Business Media, 1989).
[65] E. Vigmond, F. Vadakkumpadan, V. Gurev, H. Arevalo, M. Deo, G. Plank, and N. Trayanova, Towards predictive modelling of the electrophysiology of the heart, Experimental physiology **94**, 563 (2009).

[66] N. A. Trayanova, Whole-heart modeling: applications to cardiac electrophysiology and electromechanics, Circulation research **108**, 113 (2011).
[67] O. Smiseth and J. Aalen, Mechanism of harm from left bundle branch block, Trends in Cardiovascular Medicine **29(6)**, 335 (2019).
[68] J. M. Ferrero, B. Trenor, and L. Romero, Multiscale computational analysis of the bioelectric consequences of myocardial ischaemia and infarction, Europace **16**, 405 (2014).
[69] W. A. Ramírez, A. Gizzi, K. L. Sack, J. M. Guccione, and D. E. Hurtado, In-silico study of the cardiac arrhythmogenic potential of biomaterial injection therapy, Scientific Reports **10**, 12990 (2020).
[70] G. Del Corso, R. Verzicco, and F. Viola, Sensitivity analysis of an electrophysiology model for the left ventricle, Journal of the Royal Society Interface **17**, 20200532 (2020).